A Dissertation Submitted for a Doctorate in Materials Science

Plasmonic Nanoengineering in Hollow Metal Nanostructures: An Electron Energy-Loss Spectroscopy Study

Aziz Genç

Supervisor: Prof. Jordi Arbiol i Cobos

Tutor: Dr. Xavier Granados i García

Universitat Autònoma de Barcelona
Department of Physics, Faculty of Sciences

Institut de Ciència de Materials de Barcelona (ICMAB-CSIC)
Institut Català de Nanociència i Nanotecnologia (ICN2)

July 2015

Chapter 4

Plasmonic Nanoengineering in 1D Hollow Nanostructures: AuAg Nanotubes

4.1 Introduction

In this chapter, the plasmonic properties of metal nanotubes are presented. Bimetallic AuAg nanotubes are synthesized via galvanic replacement process where the Ag nanowires are used as a template resulting in the formation of nanotubes [69, 299], which is quite similar to the above presented nanobox synthesis. We have prepared two different samples consisting of completely hollow and hybrid AuAg nanotubes, respectively. The hybrid nanotubes are a sequence formation of solid Ag core with AuAg alloyed shell and hollow AuAg parts. The samples are deposited on 15 nm thick Si_3N_4 grids and their plasmonic properties are investigated by means of EELS spectrum imaging (SI) [206], in a monochromated STEM operated at 80 kV. In addition to the plasmonic properties, we present structural features of the completely hollow AuAg nanotubes and hybrid AuAg nanotubes by means of HRTEM investigations. Detailed STEM-EDX characterization of the hybrid AuAg nanotubes are also presented. Since the plasmonic properties of Ag nanorods/nanowires by using EELS are intensively studied in the literature [212–215, 257, 300], we directly start by the characterization of AuAg nanotubes. We compare the plasmonic properties obtained by Gaussian fitting and vertex component analysis (VCA) for both nanotube samples. BEM simulations on 1D nanostructures are conducted in order to elucidate the plasmonic properties of solid nanowires and hollow nanotubes. We could only conduct BEM simulations on the completely hollow AuAg nanotubes as the investigated hybrid nanotube has a more complex structure and longer size. It would require too complex models which are out of our computing possibilities at the moment. Nevertheless, we do not discard to work on such a demanding models in the near future.

Localized surface plasmon resonances have the ability to direct and enhance radiative emission (and vice versa) in transmission mode and they can convert propogating free-space EM wave to highly confined and strongly enhanced electric fields [120–125]. Plasmonic nanostructures can be termed as nanoantennas as their EM modulation mechanism is quite similar to the radio antennas [120, 121]. Gold and silver nanostructures are known to be promising nanoantennas with their good metallic properties and low absorption [123]. Thanks to their ability to convert light into highly localized fields, plasmonic nanoantennas have been used in many different applications. For instance, they are known to enhance the performance of different photoactive devices such as solar cells and photodetectors [128, 301]. They are also widely used in nanophotonic circuits as they are able to modify the amount and direction of the emitted electromagnetic energy [302–304]. We believe that these novel AuAg nanotubes can be good alternatives to the above-mentioned applications as they possess enhanced plasmonic properties compared to their solid counterparts.

4.2 Completely hollow AuAg nanotubes

4.2.1 Structural characterization

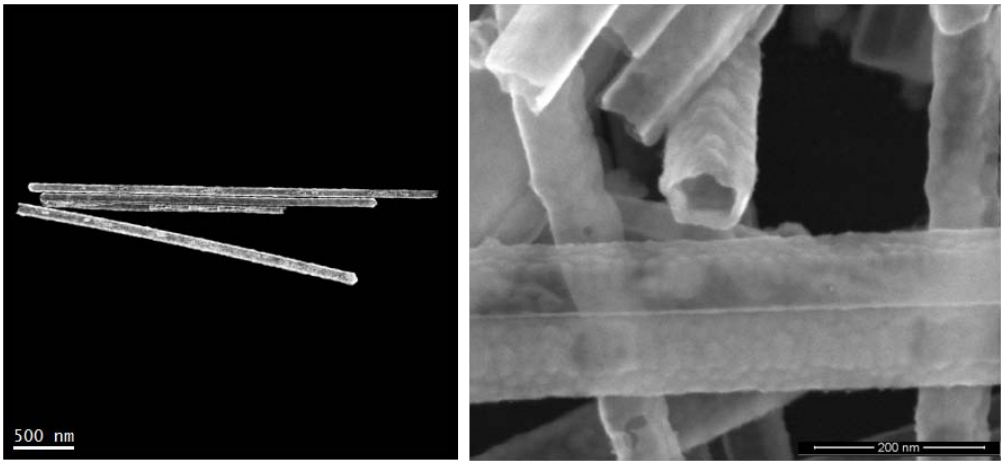

FIGURE 4.1: HAADF STEM and SEM micrographs of AuAg nanotubes, revealing the hollow and multitwinned nature of the nanotubes.

Figure 4.1 shows a HAADF STEM (left) and a SEM (right) micrographs taken from the AuAg nanotubes, revealing that perfect hollow 1D structures with micron scale lengths and $\sim$ 100 nm diameters are succesfully synthesized from the Ag nanowires after the galvanic replacement of Ag with Au. As observed in the HAADF STEM micrograph, nanotubes have faceted tips and the SEM micrograph on the right clearly reveals that these nanotubes are pentatwinned. It is very-well known that Ag nanowires synthesized via polyol techniques keep the decahedral shape of the seed nanoparticles and grow to be multiwinned [49, 51]. It is clearly evident from the SEM micrograph presented in Fig. 4.1 that the synthesized nanotubes preserve the multitwinned pentagonal shape of the Ag nanowires.

Fig. 4.2 shows several HRTEM micrographs taken from a $\sim$80 nm completely hollow nanotube shown in the low magnification TEM micrograph presented in the upper left of the figure. This nanotube may not be the same one where we have conducted the EELS measurements on (see in the Fig. 4.3A). However, they are quite similar to one another, in size and morphology and the conclusions derived from this nanotube are valid for the nanotube in Fig. 4.3A. It is seen that the nanotube is perfectly crystalline yet the fact that it is composed of a multitwinned structure that makes impossible to obtain a straightforward characterization of the phases and orientations from the HRTEM micrographs due to the overlapping of different facets of the nanotube. The investigated nanotube has an average wall thickness of around 10 nm, which varies between 7 and 13 nm and contains some voids/holes throughout the nanotube.

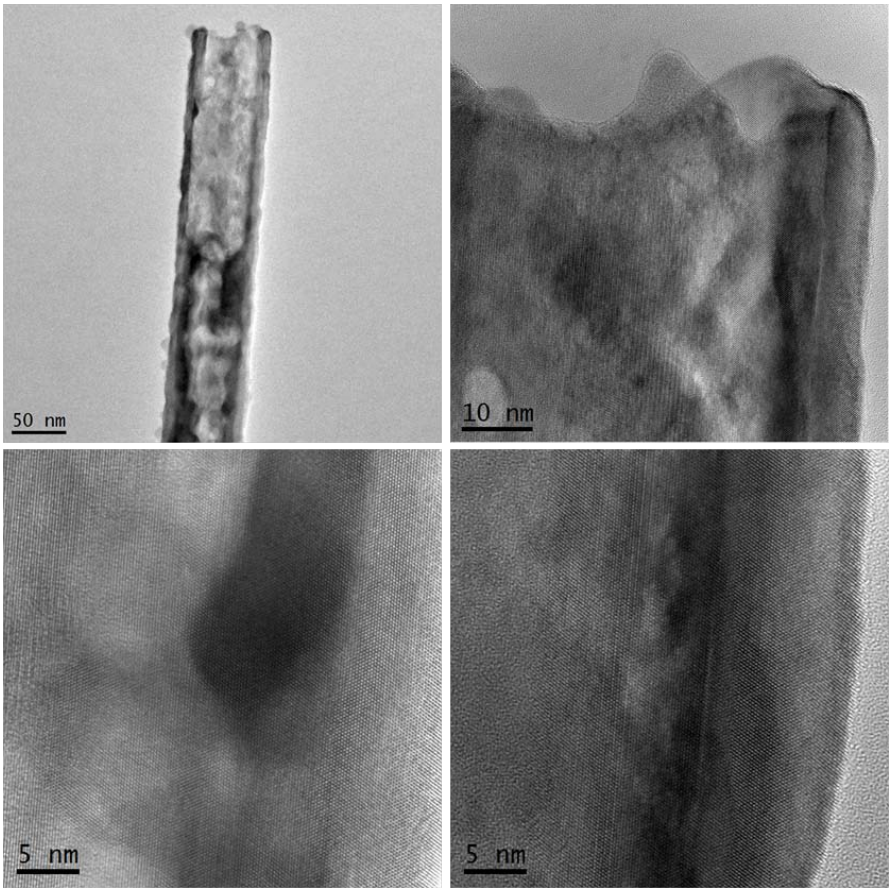

FIGURE 4.2: HRTEM micrographs of a completely hollow AuAg nanotube, showing the crystallinity of the nanotubes.

4.2.2 Local plasmonic properties

The chosen nanotube for EELS measurement is relatively shorter compared to those presented in Fig. 4.1, presenting a length of 665 nm and a diameter of 84 nm (Fig. 4.3A). Fig. 4.3B shows background subtracted selected area EEL spectra of different locations indicated in Fig. 4.3C, which is the EELS SI obtained from the region marked with white rectangle in Fig. 4.3A. It should be stressed here that one needs to take extra precautions while applying background subtraction routine by using the power law [234] as the energy of the plasmon peaks are close to the zero-loss peak. As seen in Fig. 4.3B, localized surface plasmon resonances with energies as low as ∼0.5 eV are observed for this AuAg nanotube along with several other modes at ∼0.9 eV, ∼1.2 eV, ∼1.45 eV, ∼1.7 eV, ∼2.2 eV and ∼2.54 eV.

4.2.3 Processing of plasmonic properties

In Fig. 4.4 plasmon energy and intensity maps of 5 different plasmon modes obtained by fitting a Gaussian to the energy ranges between 0.45-0.60 eV, 0.8-1.1 eV, 1.1-1.5

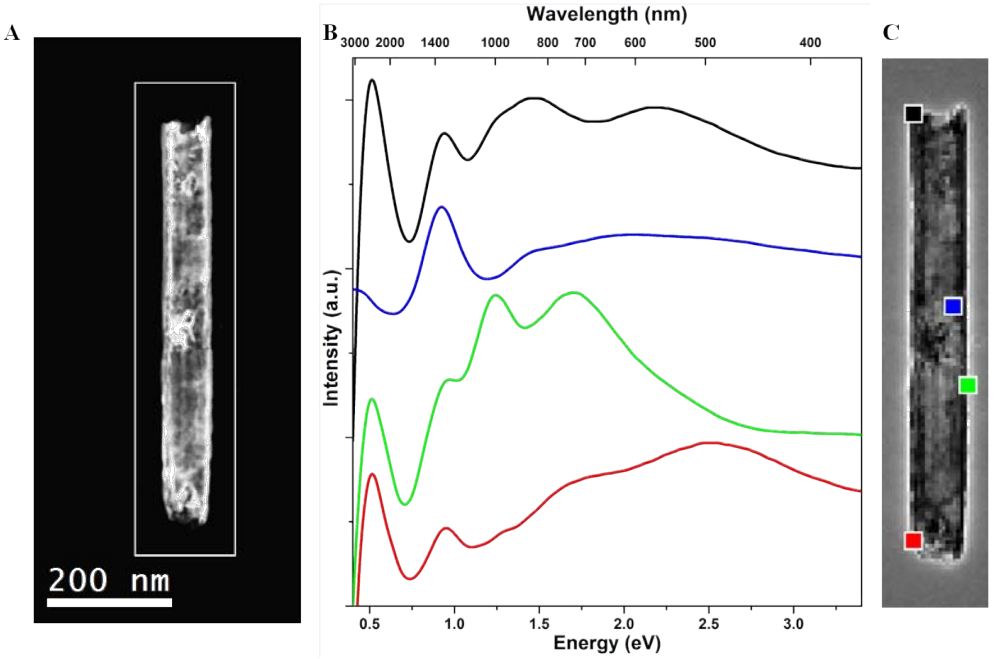

FIGURE 4.3: A. HAADF STEM micrograph of a AuAg nanotube, which is 84 nm in diameter and 665 nm in length. B. Background subtracted selected area EEL spectra of different locations marked in C, which is the EELS SI taken from the white rectangle in A.

eV, 1.5-2.3 eV and 2.3-3.1 eV are presented. As seen in these maps, Fabry-Perot type resonator resonances from $\omega = 1$ to 3 are clearly observed for the AuAg nanotube [214, 300, 305]. The first order Fabry-Perot type resonance is mapped between 0.45 and 0.60 eV and plasmon energy and intensity maps show the distribution of this mode quite clearly. Second order mode is mapped between 0.8 and 1.1 eV and the third order mode is mapped between 1.1 and 1.5 eV. Along with these Fabry-Perot type resonator resonances, two LSPR modes are mapped between 1.5 and 2.3 eV and 2.3 and 3.1 eV, revealing that the first LSPR mode may be a mode formed by merging of resonator modes and LSPR modes whereas the second LSPR mode is highly localized at certain parts of the nanotube probably due to the chemical segregation at these locations.

We have applied spectral unmixing by using vertex component analysis (VCA) algorithm to the EELS datasets obtained from the AuAg nanotubes and Fig. 4.5 shows 5 different plasmon components and their corresponding abundance maps obtained by applying VCA analysis to the EELS data of the completely hollow AuAg nanotube. Spectra of 5 components and their corresponding abundance maps are shown in these figure. Similar to the above presented Gaussian fitting results, plasmon components obtained by VCA reveal the presence of Fabry-Perot type resonator modes and LSPR for the AuAg nanotube. First, second and third order modes (components I, II and III) are located at 0.5 eV, 0.9 eV and 1.2 eV, respectively. It should be emphasized here that Fabry-Perot resonances seem to be mostly intense inside the nanotube, which is clearly

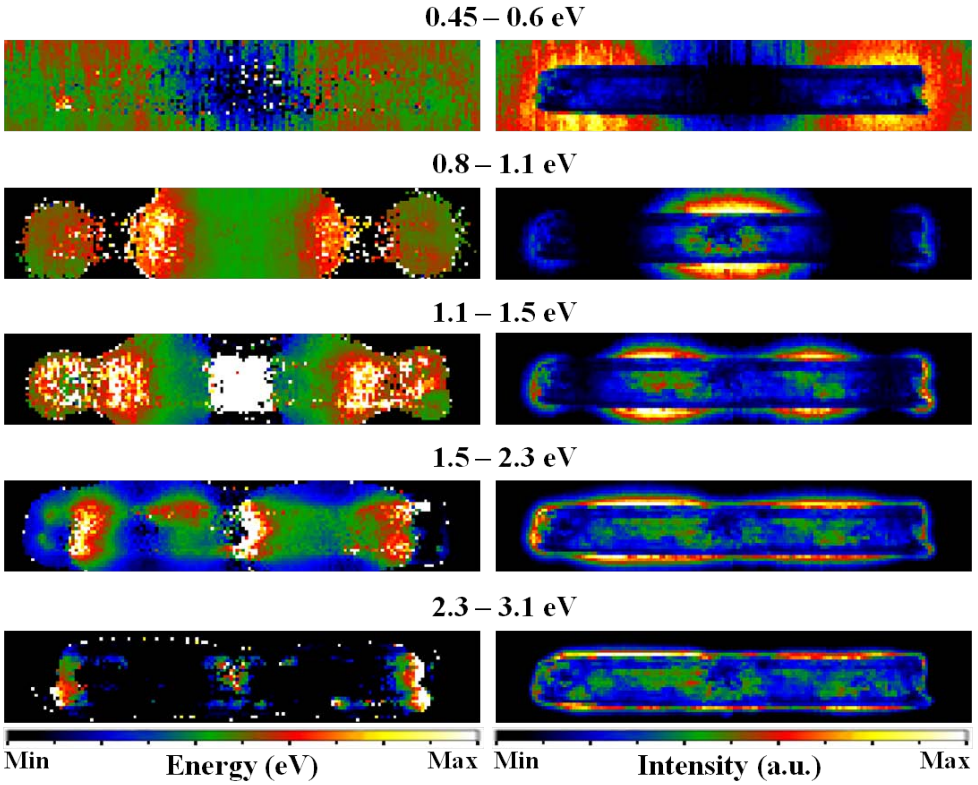

FIGURE 4.4: Plasmon energy maps (left) and their corresponding intensity maps (right) obtained by fitting a Gaussian to the energy ranges between 0.45-0.6 eV, 0.8-1.1 eV, 1.1-1.5 eV, 1.5-2.3 eV and 2.3-3.1 eV. White pixels in the energy maps are parameters out of fitting.

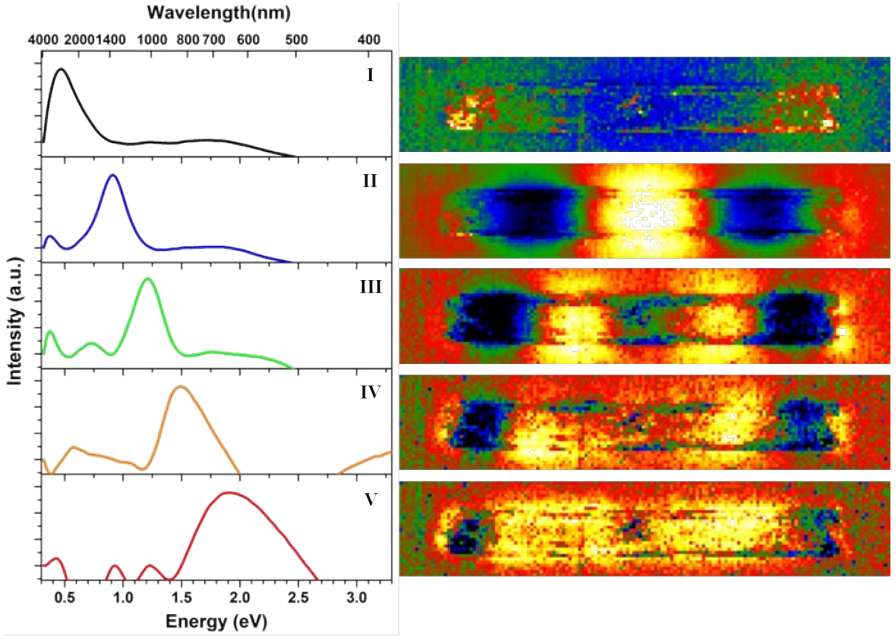

FIGURE 4.5: VCA of the completely hollow AuAg nanotube: Plasmon components and their corresponding abundance maps.

revealed in the abundance maps of components II (second order mode) and III (third order mode). By looking the abundance map of the component IV, which is located at 1.5 eV, one can suggest that this mode is more like a fourth order mode than a LSPR mode. A wide peak at 1.9 eV (component V) is associated with a LSPR mode and its corresponding abundance map shows its distribution throughout the nanotube.

4.2.4 Boundary element method (BEM) simulations

We continue with the simulations of plasmonic properties in 1D metal nanostructures. Although we did not conduct EELS experiments on Ag nanowires as their properties widely studied in literature, we simulate the plasmonic properties of an Ag nanowire having same sizes as the completely hollow AuAg nanocube as a reference.

4.2.4.1 BEM simulations on an Ag nanowire standing in vacuum

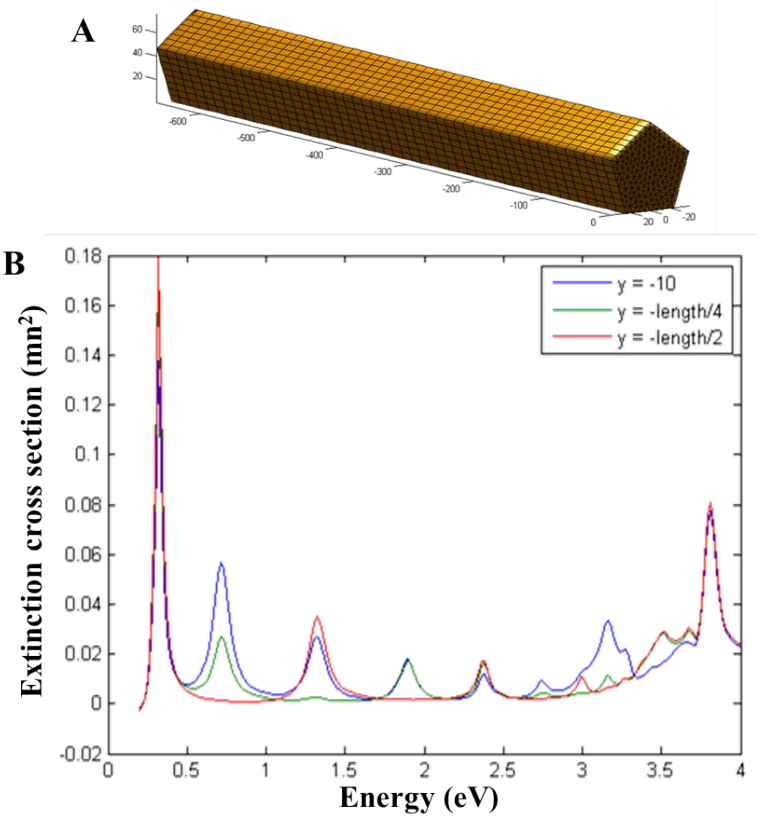

FIGURE 4.6: A. Structural model of the BEM simulated Ag nanowire with a length of 665 nm and a diameter of 84 nm. B. Simulated local EEL spectra obtained at the tip, at a quarter of the length (at $\sim$ 166 nm) and at the center (at 332.5 nm) of the Ag nanowire. Note that the nanowire is standing in vacuum.

Fig. 4.6A shows the structural model of the Ag nanowire that is used for the BEM simulations. The simulated nanowire has a pentagonal morphology with the same sizes of

a 665 nm length and 84 nm diameter as the experimentally investigated, above presented, completely hollow AuAg nanotube. It should be noted here that the Ag nanowire is standing in vacuum. Fig. 4.6B shows the BEM simulated EELS spectra obtained at the tip (near the edge, in blue), at the one quarter of the nanowire length (at ∼166 nm, in green) and at the center (at 332.5 nm, in red) of the nanowire. As seen in these EEL spectra, presence of several peaks are observed at the different locations of the Ag nanowire. At the first instance, the presence of at least 12 peaks can be observed, which are located at ∼0.31 eV, ∼0.71 eV, ∼1.32 eV, ∼1.89 eV, ∼2.38 eV, ∼2.74 eV, ∼2.99 eV, ∼3.16 eV, ∼3.28 eV, ∼3.52 eV, ∼3.68 eV and ∼3.8 eV. The lowest energy peak is located at ∼0.31 eV and it is present in all three locations. Second peak located at ∼0.71 eV is present at the tip with high intensity and at the quarter length with lower intensity. A third peak located at ∼1.32 eV is present at the tip and at the center of the nanowire. The periodicty of the peak locations for some of the peaks listed above suggests the presence of Fabry-Perot resonator type modes, which is quite expected for a Ag nanowire as discussed above. The plasmon maps presented in the following will reveal the nature of these peaks.

BEM simulated plasmon maps of 12 different peaks located at 0.314 eV, 0.713 eV, 1.321 eV, 1.891 eV, 2.385 eV, 2.746 eV, 2.993 eV, 3.164 eV, 3.278 eV, 3.525 eV, 3.677 eV and 3.81 eV in Fig. 4.6B are shown in Fig. 4.7. The plasmon map of the lowest energy peak located at 0.314 eV shows that this mode is present all over the nanowire. Plasmon modes with such distributions are termed as dark plasmonic breathing modes with an analogy to acoustic vibrations [218]. To the best of our knowledge, presence of such a plasmon mode in Ag nanowires is not reported previously. It should be noted again that these simulation results are obtained for an Ag nanowires standing in vacuum, and the presence of a substrate may cause the absorption of this mode located at a low energy of 0.314 eV. This may be the reason that presence of such a mode could not observed experimentally in the literature. It is also interesting to point out that we do not observe this mode during the simulations of Ag nanotubes or AuAg nanotubes presented in the following. We are still working on the complementary simulations in order to understand the origin of its presence. The plasmon maps of the modes at 0.713 eV, 1.321 eV, 1.891 eV, 2.385 eV, 2.746 eV and 2.993 eV reveal that these modes are Fabry-Perot type resonator modes with $\omega = 1$, 2, 3, 4, 5 and 6, respectively. Distributions of two different multipolar localized surface plasmon resonance modes located at 3.164 eV and 3.278 eV are shown in this figure. The distributions of the modes located at 3.525 eV and 3.677 eV are not conclusive enough to define the nature of these modes, which may be LSPR modes or high order Fabry-Perot resonator modes. Finally, the bulk plasmon mode of Ag is shown at 3.81 eV.

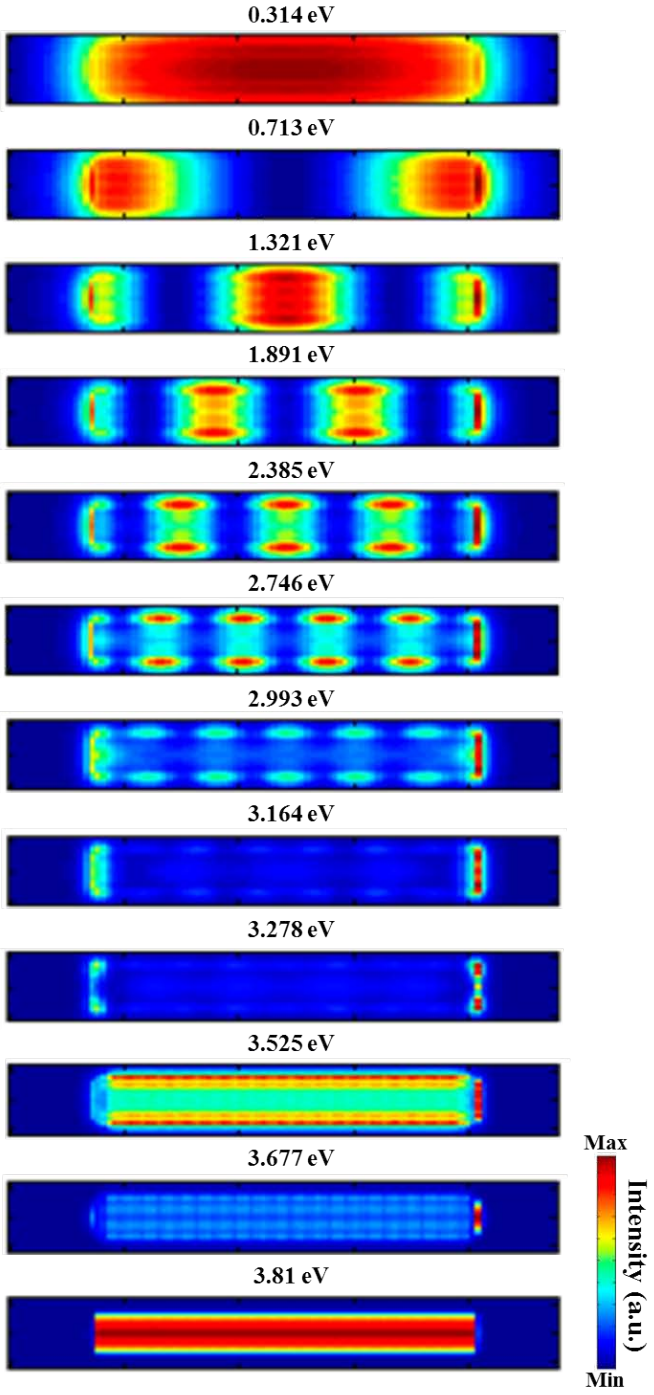

FIGURE 4.7: BEM simulated plasmon maps of the Ag nanowire: Maps of 12 different modes, located at 0.314 eV, 0.713 eV, 1.321 eV, 1.891 eV, 2.385 eV, 2.746 eV, 2.993 eV, 3.164 eV, 3.278 eV, 3.525 eV, 3.677 eV and 3.81 eV, are presented.

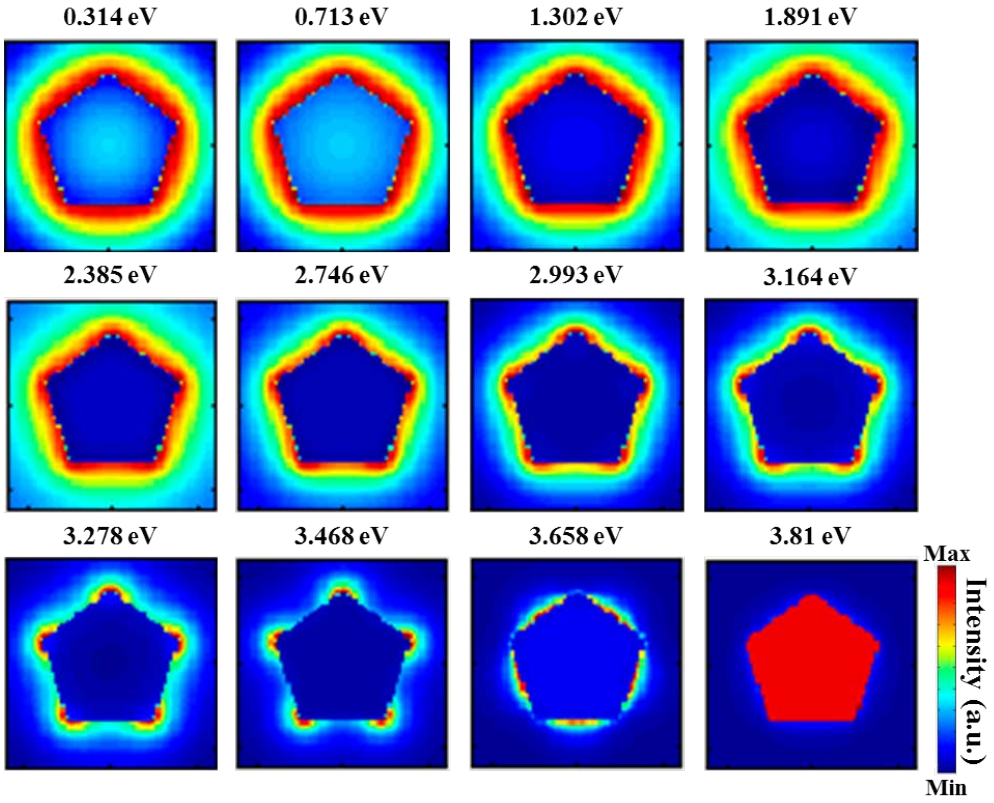

FIGURE 4.8: BEM simulated plasmon maps of the Ag nanowire obtained by the beam incident on the pentagonal cross-section: Maps of 12 different modes, located at 0.314 eV, 0.713 eV, 1.302 eV, 1.891 eV, 2.385 eV, 2.746 eV, 2.993 eV, 3.164 eV, 3.278 eV, 3.468 eV, 3.658 eV and 3.81 eV, are presented. Note that 3 of the modes located at 1.302 eV, 3.468 and 3.658 eV have slightly different energies than those presented in Fig. 4.7.

Fig. 4.8 shows the BEM simulated plasmon maps of Ag nanowire from the cross-sectional view. The maps are obtained by the beam incident on the pentagonal cross-section of the nanowire. Plasmon maps of 12 different modes located at 0.314 eV, 0.713 eV, 1.302 eV, 1.891 eV, 2.385 eV, 2.746 eV, 2.993 eV, 3.164 eV, 3.278 eV, 3.468 eV, 3.658 eV and 3.81 eV are presented in this figure. Note that 3 of these modes, located at 1.302 eV, 3.468 eV and 3.658, have slightly different energy than those obtained from the planar view (Fig. 4.7), which are located at 1.321 eV, 3.525 eV and 3.677 eV, respectively. This may be due to some numerical accuracy issues or due to the excitation angle of the beam and the same modes being generated with slightly different energies. These cross-sectional plasmon maps clearly reveal that the breathing mode located at 0.314 eV and the Fabry-Perot resonator modes, located at 0.713 eV, 1.302 eV, 1.891 eV, 2.385 eV, 2.746 eV and 2.993 eV, have a homogeneous distribution around the section nanowire. Nevertheless, it should be noted that the high order Fabry-Perot resonator modes have slightly higher intensities at the corners (vertexes) of the pentagon. Cross-sectional maps of the LSPR modes located at 3.164 eV, 3.278 eV and 3.468 eV reveal that these modes

are highly confined at the corners. The mode located at 3.658 eV can be identified as a face mode. It is worth noting that these cross-sectional plasmon maps allow us to identify the modes located at 3.468 eV and 3.658 eV as LSPR modes, which, or their possible correspondents located at 3.525 eV and 3.677 eV, could not be determined along the planar view. As expected, the bulk plasmon mode of the Ag located at 3.81 eV is present all around the cross-section.

As a summary of the modes mentioned above, Table 4.1 shows the list of 12 different modes observed during the BEM simulations on the Ag nanowire. Note that we have used the resonance energy values obtained from the planar view and, as discussed above, some of the modes may have slightly different energies along the cross-section.

TABLE 4.1: A list of resonance energies and resonance types for 12 different modes observed during the BEM simulations on the Ag nanowire.

Resonance energy	**Resonance type**
0.314 eV	Dark plasmonic breathing mode
0.713 eV	Fabry-Perot, 1^{st} order
1.321 eV	Fabry-Perot, 2^{nd} order
1.891 eV	Fabry-Perot, 3^{rd} order
2.385 eV	Fabry-Perot, 4^{th} order
2.746 eV	Fabry-Perot, 5^{th} order
2.993 eV	Fabry-Perot, 6^{th} order
3.164 eV	LSPR, corner/edge
3.278 eV	LSPR, corner
3.525 eV	LSPR, corner
3.677 eV	LSPR, face
3.81 eV	Bulk

4.2.4.2 BEM simulations on an Ag nanotube standing in vacuum

Fig. 4.9A shows the structural model of the Ag nanotube that is used for the BEM simulations in order to have a better understanding about the differences between solid and hollow 1D nanostructures. The simulated nanotube also has a pentagonal morphology with the same sizes of a 665 nm length and 84 nm diameter with a 10 nm thick continuous wall. It is standing in vacuum. Fig. 4.9B shows the BEM simulated EELS spectra obtained at the tip (near the edge, in blue), at the one quarter of the nanotube length (at ∼166 nm, in green) and at the center (at 332.5 nm, in red) of the nanotube. At the first instance, one can see that the breathing plasmon mode observed for the

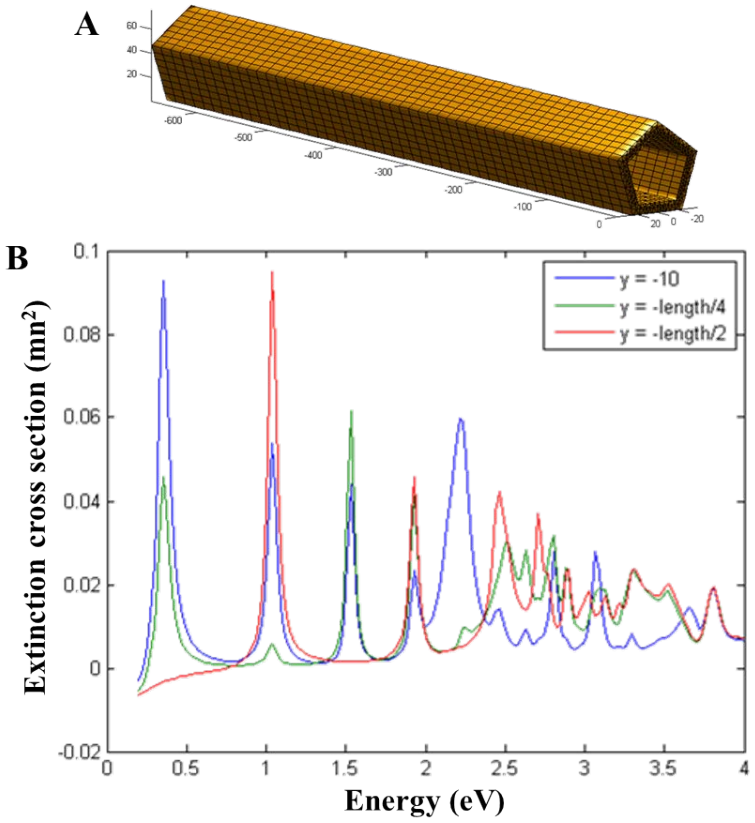

FIGURE 4.9: A. Structural model of the BEM simulated Ag nanotube with a length of 665 nm and a diameter of 84 nm. B. Simulated local EEL spectra obtained at the tip, at a quarter of the length (at ∼ 166 nm) and at the center (at 332.5 nm) of the Ag nanotube. Note that the nanotube is standing in vacuum.

Ag nanowire is not present at the BEM simulated EEL spectra of the Ag nanotube. Moreover, it is clear that plasmon resonances shifted to lower energies compared to solid Ag nanowire due to plasmon hybridization between solid and cavity modes [63]. As seen in these EEL spectra, presence of several peaks are observed at the different locations of the Ag nanotube. Some high intensity peaks are located at ∼0.35 eV, ∼1.0 eV, ∼1.5 eV, ∼1.9 eV, ∼2.2 eV, ∼2.4 eV and ∼2.6 eV, along with the several low intensity peaks located between 2.3 eV and 3.8 eV. It should be pointed out here that we did not take the instrumental broadening into account during these BEM simulations. Some of these peaks with very similar energy values would merge together in the experimental EELS measurements.

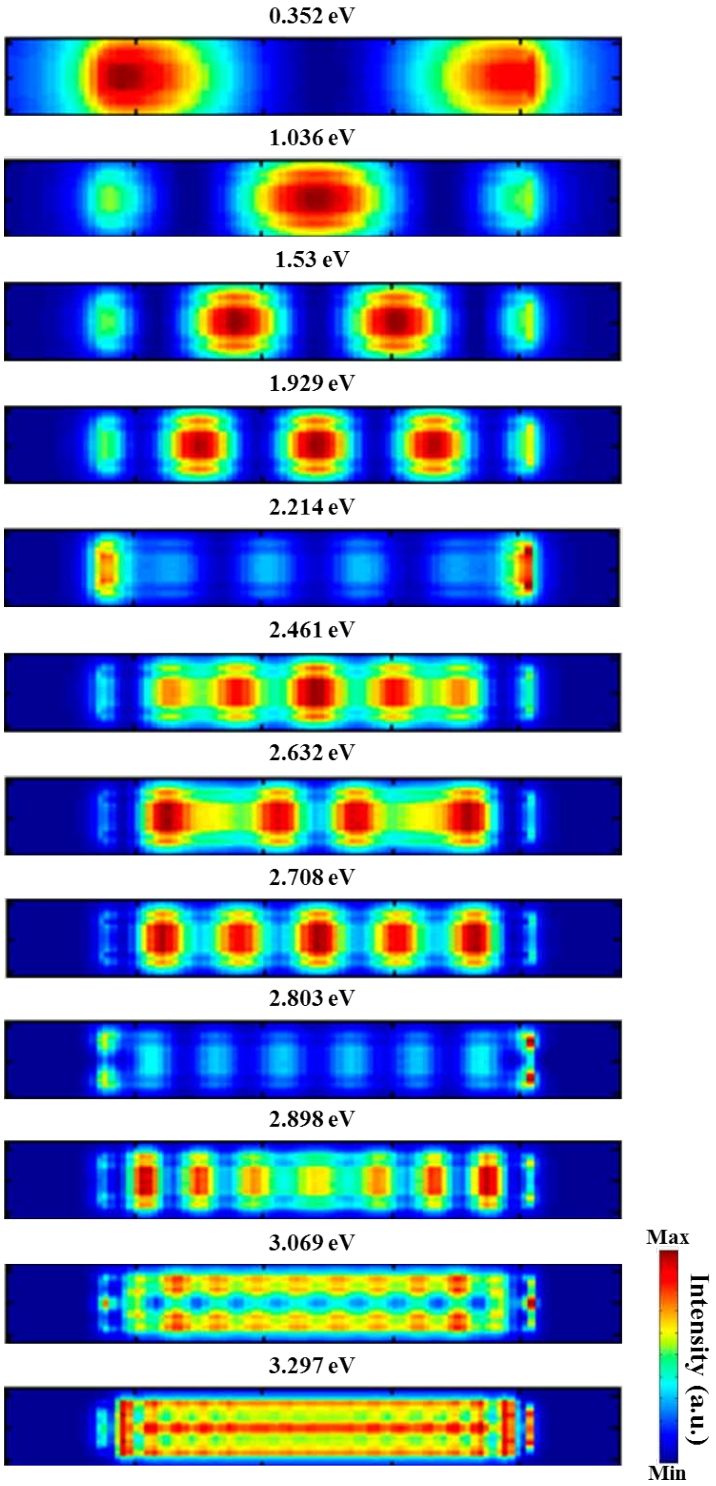

FIGURE 4.10: BEM simulated plasmon maps of the Ag nanotube: Maps of 12 different modes, located at 0.352 eV, 1.036 eV, 1.53 eV, 1.929 eV, 2.214 eV, 2.461 eV, 2.632 eV, 2.708 eV, 2.803 eV, 2.898 eV, 3.069 eV and 3.297 eV, are presented.

BEM simulated plasmon maps of 12 different peaks located at 0.352 eV, 1.036 eV, 1.53 eV, 1.929 eV, 2.214 eV, 2.461 eV, 2.632 eV, 2.708 eV, 2.803 eV, 2.898 eV, 3.069 eV and 3.297 eV in Fig. 4.9B are shown in Fig. 4.10. The mode located at 0.352 eV is

the first order Fabry-Perot type resonator mode, which was located at 0.713 eV for the solid Ag nanowire. Such a shift reveal the effects of the plasmon hybridization in hollow nanostructures, which was discussed throughly in the previous chapter. For instance, we have showed the shifts of plasmon peaks in cubic Ag nanostructures with increasing void sizes in Fig. 3.27. Similar behaviour is observed in the case of 1D nanostructures presented here. The distributions of second, third and fourth order Fabry-Perot modes located at 1.036 eV, 1.53 eV and 1.929 eV, respectively, are clearly seen in this BEM simulated plasmon maps. It should be noted here that these Fabry-Perot resonator modes are most efficiently excited at the inside of the nanotube. The LSPR mode located at 3.164 eV in the solid Ag nanowire shifted significantly to 2.214 eV in the hollow Ag nanotube, which is highly confined at the tips of the nanotube. The nature of the modes located at 2.461 eV, 2.708 eV and 2.898 eV is not clear in these plasmon maps, i.e. they are most probably high order Fabry-Perot modes, yet they may be LSPR modes as well. In any case, it is clear that they have intense resonances both at the inner and outer parts of the nanotube. Similarly, a LSPR mode located at 2.632 eV have high intensities at the inner and outer parts of the nanotube. Another LSPR mode located at 2.803 eV is mostly confined at the tips with some contributions from the other parts of the nanotube. The plasmon maps of the modes located at 3.069 eV and 3.297 eV reveals that these modes have multipolar contributions. The fact that hollow 1D nanostructures have highly intense Fabry-Perot type and LSPR modes both at the inner and outer parts of the nanostructure suggest that they can be good alternatives in different applications of plasmonic nanoantennas [120, 121, 123].

Fig. 4.11 shows the BEM simulated plasmon maps of Ag nanotube from the cross-sectional view. The maps are obtained by the beam incident on the pentagonal cross-section of the nanotube. Plasmon maps of 12 different modes located at 0.352 eV, 1.036 eV, 1.53 eV, 1.929 eV, 2.233 eV, 2.461 eV, 2.632 eV, 2.708 eV, 2.803 eV, 2.879 eV, 3.126 eV and 3.305 eV are presented in this figure. Note that energy of some of these modes are slightly different than those obtained along the planar view (Fig. 4.7). These cross-sectional plasmon maps clearly reveal that the Fabry-Perot resonator modes, located at 0.352 eV, 1.036 eV, 1.53 eV and 1.929 eV have a homogeneous distribution of highly intense plasmon resonances all around, i.e. inner and outer parts, of the nanotube section. Cross-sectional maps of the LSPR modes located at 2.233 eV and 2.461 eV also reveal similar homogeneous distribution with slightly lower intensities at the center of the void. The cross-section maps of the modes located at 2.632 eV, 2.708 eV, 2.803 eV, 2.879 eV and 3.126 eV reveal that these modes are confined around the inner and outer parts of the nanotube wall. It should be pointed out here that these 7 different modes are distributed homogeneously around the nanotube with no side-specific, i.e. corners, faces, confinement. As discussed in detail in the Chapter 3, this is due to the

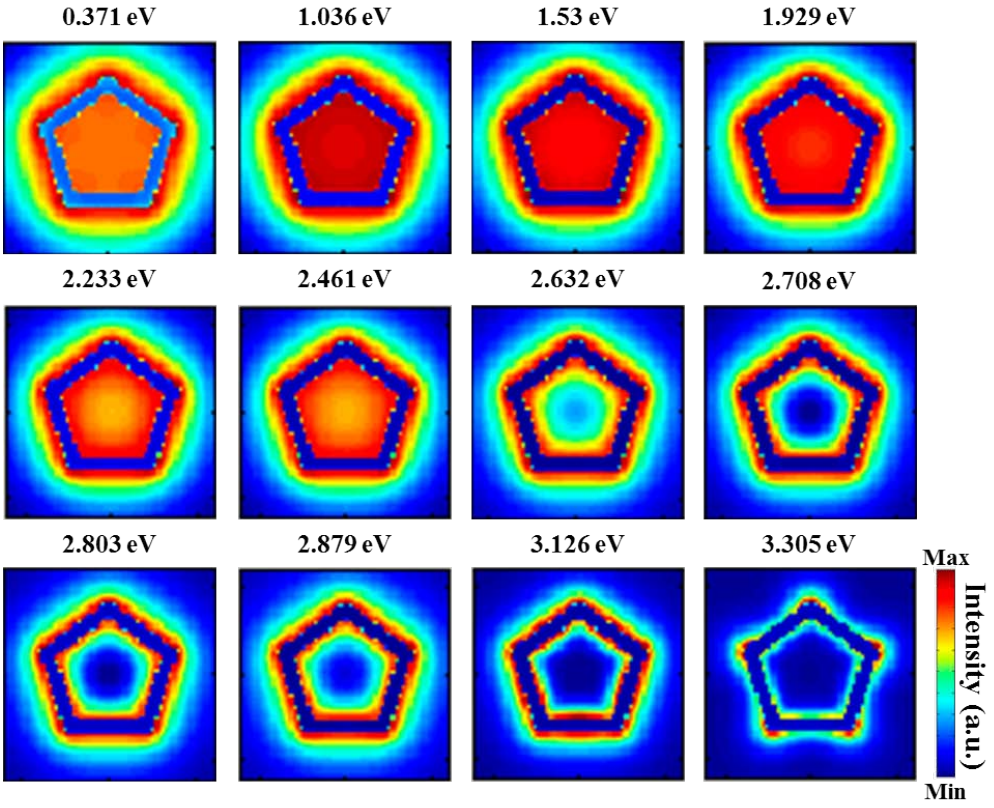

FIGURE 4.11: BEM simulated plasmon maps of the Ag nanotube obtained by the beam incident on the pentagonal cross-section: Maps of 12 different modes, located at 0.352 eV, 1.036 eV, 1.53 eV, 1.929 eV, 2.233 eV, 2.461 eV, 2.632 eV, 2.708 eV, 2.803 eV, 2.879 eV, 3.126 eV and 3.305 eV, are presented. Note that energy of some of the modes are slightly different than those presented in Fig. 4.10.

coupling of inner and outer resonances of the nanotube which creates a homogeneously distributed plasmon resonances [61, 63, 140]. Finally, the mode located at 3.305 eV is highly confined at the corners of the pentagon. Again, we should note that the nanotubes are simulated as having perfect pentagon structures but the synthesized nanotube have more rounded vertexes (Fig. 4.1). Therefore, we assume that such a confinement at the corners/vertexes would not be the case for nanotubes with smoother corners. It was the case for the single-walled AuAg nanoboxes presented in Chapter 3, where the plasmon mode confined at the corners of a sharp nanobox was distributed around the corners and edges for a nanobox with rounded corners (see Fig. 3.33 and Fig. 3.36).

As a summary, we present the list of 12 different modes obtained during the BEM simulations of the Ag nanotube in Table 4.2, where we have labeled LSPR modes without specifying the location as they are homogeneously distributed around the nanotube.

TABLE 4.2: A list of resonance energies and resonance types for 12 different modes observed during the BEM simulations on the Ag nanotube.

Resonance energy	**Resonance type**
0.352 eV	Fabry-Perot, 1^{st} order
1.036 eV	Fabry-Perot, 2^{nd} order
1.53 eV	Fabry-Perot, 3^{rd} order
1.929 eV	Fabry-Perot, 4^{th} order
2.214 eV	LSPR
2.461 eV	LSPR
2.632 eV	LSPR
2.708 eV	LSPR or Fabry-Perot, 6^{th} order
2.803 eV	LSPR
2.898 eV	LSPR
3.069 eV	LSPR
3.297 eV	LSPR, corner

4.2.4.3 BEM simulations on an Ag nanotube standing on substrate

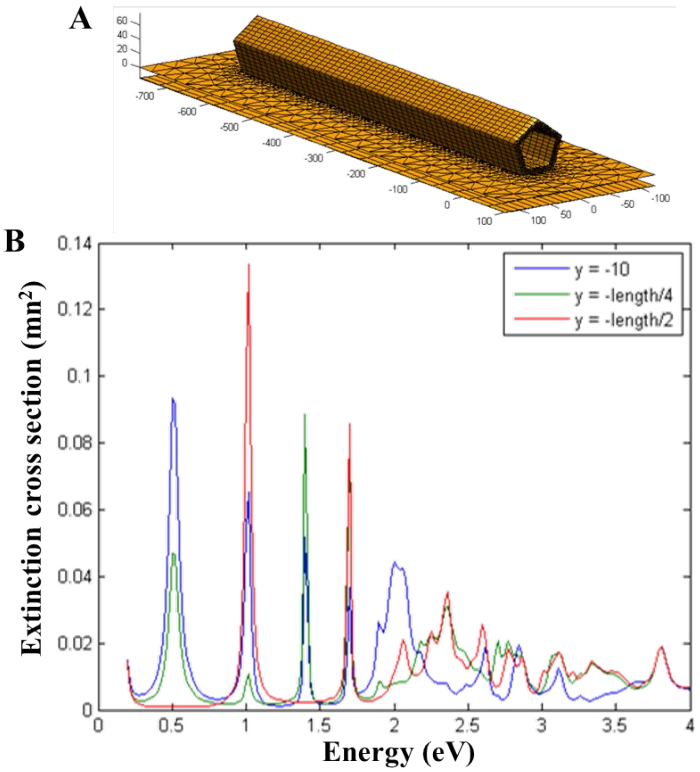

FIGURE 4.12: A. Structural model of the BEM simulated Ag nanotube with a length of 665 nm and a diameter of 84 nm, with 10 nm thick walls, standing on a 15 nm thick Si_3N_4 substrate. B. Simulated local EEL spectra obtained at the tip, at a quarter of the length (at $\sim$ 166 nm) and at the center (at 332.5 nm) of the Ag nanotube.

After revealing the differences between a solid and hollow 1D nanostructure standing in vacuum, we continue with the addition of a substrate in order to discuss its effects on the plasmonic properties of hollow 1D nanostructures. As discussed above for the cuboid nanostructures, plasmon modes of the nanostructures interact with the sample resulting in the formation of distal and proximal modes [90, 91]. Fig. 4.12A shows the structural model of the Ag nanotube (655 nm long, 84 nm wide with 10 nm thick walls) standing on a 15 nm thick Si_3N_4 substrate, which is used during BEM simulations of the Ag nanotubes. Fig. 4.12B shows the BEM simulated EELS spectra obtained at the tip (near the edge, in blue), at the one quarter of the nanotube length (at $\sim$166 nm, in green) and at the center (at 332.5 nm, in red) of the nanotube. It is seen that all the peaks shifted to lower energies except the lowest energy peak corresponding to the first order Fabry-Perot resonator mode located at $\sim$0.52 eV, which is located at 0.352 eV for the Ag nanotube standing in vacuum. As there is no study about the plasmonic properties of hollow 1D nanostructures, we are not sure whether this is caused by a numerical accuracy or it is typical for such nanostructures. The presence of many different peaks

obtained at different parts of the Ag nanotube standing on a Si_3N_4 substrate is shown in this figure. Since there are more than 10 peaks located between 2 eV and 3.8 eV, we do not mention all the peaks with their energy values but one can easily distinguish several sharp peaks located at ∼0.52 eV, ∼1.0 eV, ∼1.4 eV, ∼1.7 eV eV, ∼2.0 eV and ∼2.4 eV among many others.

BEM simulated plasmon maps of 12 different peaks located at 0.523 eV, 1.017 eV, 1.397 eV, 1.701 eV, 1.891 eV, 2.005 eV, 2.062 eV, 2.252 eV, 2.366 eV, 2.594 eV, 2.708 eV and 2.765 eV in Fig. 4.12B are shown in Fig. 4.13. As mentioned before, the peaks shifted to lower energies in general except the one located at 0.523 eV. Its BEM simulated map shows that this is the first order Fabry-Perot resonator mode and it is mostly excited inside the nanotube. Second, third, fourth and fifth order Fabry-Perot modes, which are located at 1.017 eV, 1.397 eV, 1.701 eV and 1.891 eV, respectively, reveals the similar distribution of plasmon resonances, i.e. they are mostly intense at the inner part of the Ag nanotube along with intense presence at the outer parts. Two LSPR modes that are located at 2.005 eV and 2.062 eV are highly confined at the tips of the nanotube. As mentioned before, after taking the instrumental broadening into account, which is about 130 meV for the experimentally obtained EELS maps, these two peaks with an energy difference of 57 meV would merge together. BEM simulated plasmon maps of some other LSPR modes located at various energies are shown in this figure.

Similar to the discussions about BEM simulated plasmonic properties of cuboid AuAg nanostructures, we have used pure Ag as a playground in order to discuss the plasmonic property differences between solid and hollow 1D nanostructures and the effects of substrate presence on the plasmonic properties of the hollow 1D nanostructures. So far, we have shown that both solid (Ag nanowires) and hollow (Ag nanotubes) 1D nanostructures contain multiple Fabry-Perot type resonator modes and LSPR modes. The presence of a dark plasmonic breathing mode for the Ag nanowire is observed during the BEM simulations and we need to have a better understanding about this mode. In addition, we have observed that the energy of Fabry-Perot and LSPR modes shifted to lower energies for the hollow nanotube compared to those of the solid nanowires, due to plasmon hybridization between solid and cavity modes. It has been revealed that most of the plasmon modes (both Fabry-Perot type and LSPR) are excited most intensely from the inner parts of the hollow nanostructure. Implementation of a 15 nm thick Si_3N_4 substrate caused a furhter shift of the plasmon resonances of the Ag nanotubes to lower energies, except the first order Fabry-Perot mode which shifted to higher energies.

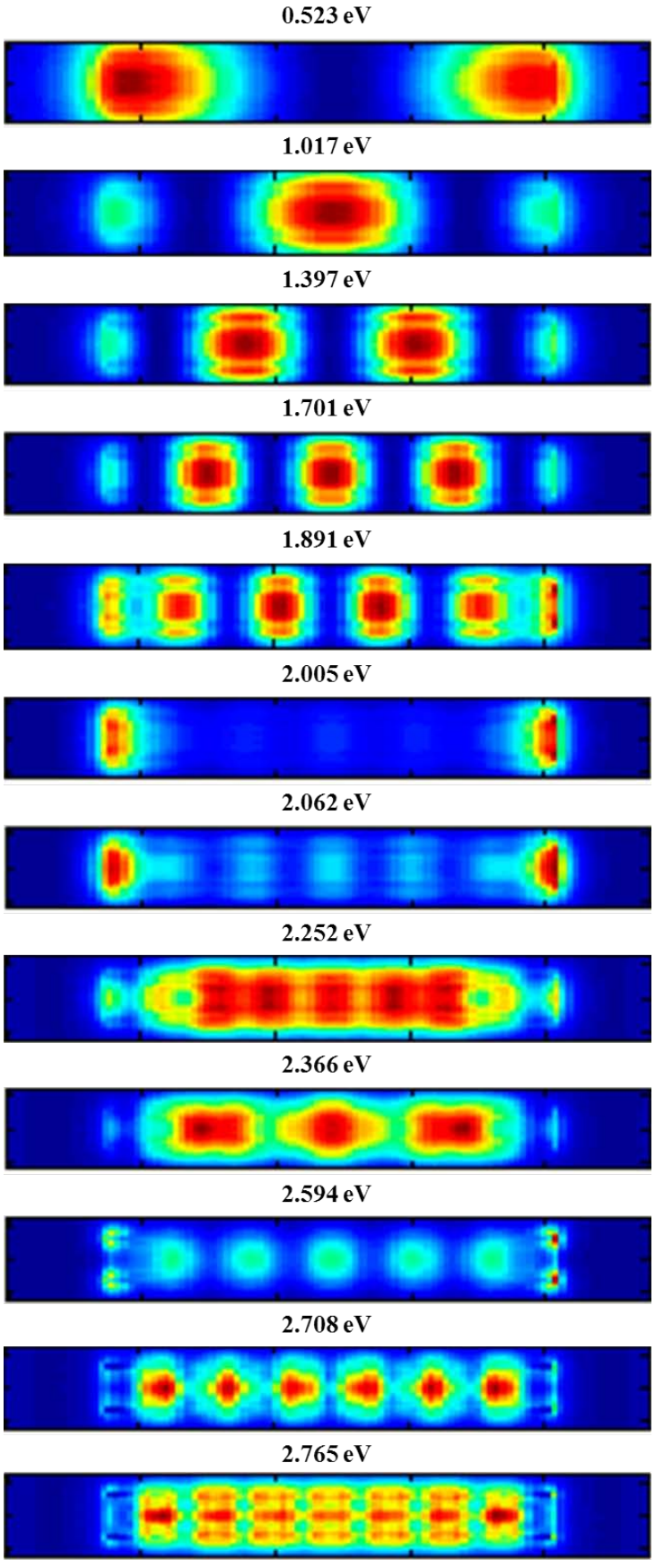

FIGURE 4.13: BEM simulated plasmon maps of the Ag nanotube standing on a Si_3N_4 substrate: Maps of 12 different modes, located at 0.523 eV, 1.017 eV, 1.397 eV, 1.701 eV, 1.891 eV, 2.005 eV, 2.062 eV, 2.252 eV, 2.366 eV, 2.594 eV, 2.708 eV and 2.765 eV, are presented.

TABLE 4.3: A list of resonance energies and resonance types for 12 different modes observed during the BEM simulations on the Ag nanotube standing on a 15 nm thick Si_3N_4 substrate.

Resonance energy	**Resonance type**
0.523 eV	Fabry-Perot, 1^{st} order
1.017 eV	Fabry-Perot, 2^{nd} order
1.397 eV	Fabry-Perot, 3^{rd} order
1.701 eV	Fabry-Perot, 4^{th} order
1.891 eV	Fabry-Perot, 5^{th} order
2.005 eV	LSPR, tip
2.062 eV	LSPR, tip
2.252 eV	LSPR
2.366 eV	LSPR
2.594 eV	LSPR
2.708 eV	LSPR
2.765 eV	LSPR, corner

Table 4.3 shows the list of resonance energies and resonance types for 12 different modes observed during the BEM simulations on the Ag nanotube standing on a 15 nm thick Si_3N_4 substrate. As, we have simulated this nanostructure, the Ag nanotube standing on a substrate, just to see the effects of substrate presence on plasmon resonance energies, we did not obtain cross-sectional maps during these simulations. Therefore, it is hard to tell the nature and distribution of the LSPR modes listed in this table. As the cross-sectional maps are presented for the following AuAg nanotube on the substrate, we can use those maps in order the determine the behavior of the LSPR modes of the nanotubes in the presence of a substrate.

4.2.4.4 BEM simulations on an AuAg nanotube standing on substrate

In light of these pre-knowledge about the plasmonic properties of the hollow 1D nanostructures, we continue the BEM simulations on an AuAg nanotube that has a chemical composition of 40 at.% Ag and 60 at.% Au. It has similar chemical composition as the experimentally investigated completely hollow AuAg nanotube. Yet, it should be noted here that we do not take the presence of voids along the walls of the nanotube into account as they have various sizes and they are randomly distributed (Fig. 4.3). In other words, we simulate the plasmonic properties of an AuAg nanotube with 10 nm

thick homogeneously continuous walls. Another assumption made is about the distribution of Ag and Au throughout the nanotube, where we have considered a homogeneous distribution all around the nanotube.

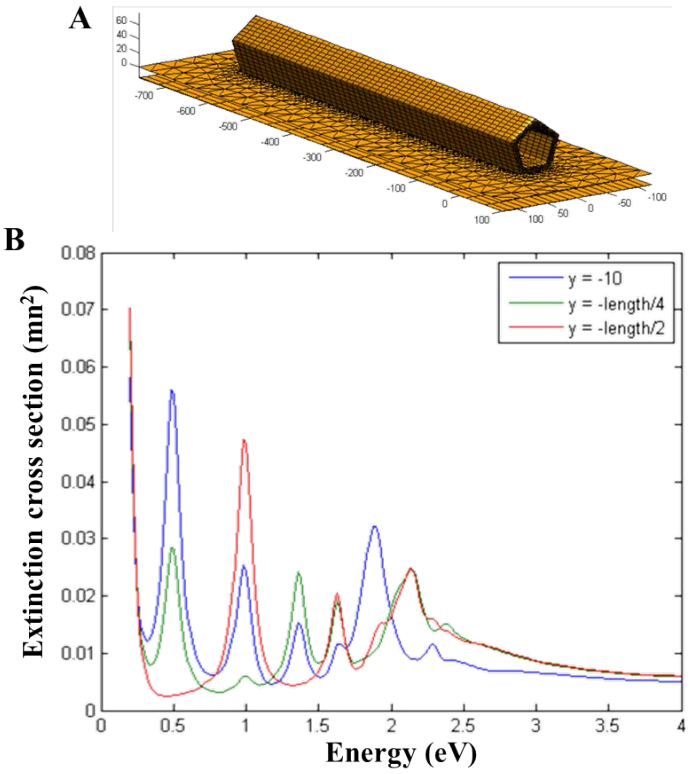

FIGURE 4.14: A. Structural model of the BEM simulated AuAg nanotube with a length of 665 nm and a diameter of 84 nm, with 10 nm thick walls, standing on a 15 nm thick Si_3N_4 substrate. B. Simulated local EEL spectra obtained at the tip, at a quarter of the length (at $\sim$ 166 nm) and at the center (at 332.5 nm) of the AuAg nanotube.

Fig. 4.14A shows the structural model of the AuAg nanotube composed of 60 at.% Au and 40 at.% Ag standing on a 15 nm thick Si_3N_4 substrate, which is used during BEM simulations of the Ag nanotubes. Similar to above presented simulations on 1D Ag nanostructures, it has similar dimensions as the experimentally investigated completely hollow AuAg nanotube. Thus, it has a length of 655 nm, a diameter of 84 nm with 10 nm thick walls. Fig. 4.14B shows the BEM simulated EELS spectra obtained at the tip (near the edge, in blue), at the one quarter of the nanotube length (at $\sim$166 nm, in green) and at the center (at 332.5 nm, in red) of the AuAg nanotube. At the first instance one can see that the energies of the peaks corresponding to Fabry-Perot resonator modes with energies less than 2 eV are more or less similar to those observed for the pure Ag nanotube in Fig. 4.12B. It is because Ag and Au have similar dielectric functions at these energy range as shown in Fig. 3.21. Another obvious feature of the simulated EEL spectra of the AuAg nanotube is that there is almost no visible peak at energies higher than 2.5 eV. The plasmon peak at high energies are diminished because

of a mechanism called plasmon damping [64], in which the overlapping of the onset of the interband transitions with the LSPRs of Au causes a decrease in LSPR intensity at higher energies [53, 64]. As seen in the simulated local EEL spectra of the AuAg nanotube, several plasmon peaks are located at ∼0.5 eV, ∼1.0 eV, ∼1.35 eV, ∼1.6 eV, ∼1.9 eV, ∼2.1 eV and ∼2.3 eV. It is worth noting that the intensity of the EELS signal below 0.5 eV increases towards lower energy, which might suggest a possible presence of a dark plasmoninc breathing-like plasmon mode at this energy range, yet it is hard to tell by just looking at these simulated EEL spectra.

BEM simulated plasmon modes of the AuAg nanotube standing on a 15 nm thick Si_3N_4 substrate are shown in Fig. 4.14. As seen in this figure, maps of 8 different modes located at 0.504 eV, 0.979 eV, 1.359 eV, 1.625 eV, 1.891 eV, 2.139 eV, 2.29 eV and 2.385 eV are presented for the AuAg nanotube. Fabry-Perot resonator modes up to fourth order are located at 0.504 eV, 0.979 eV, 1.359 eV and 1.625 eV, respectively, revealing that these modes are excited most intensely inside the nanotube. These maps obtained by BEM simulations are quite similar to the experimentally observed abundance maps of VCA (4.5), where it is shown that Fabry-Perot modes are highly intense inside the nanotube. The LSPR mode located at 1.891 eV is confined at the tips of the nanotube. Another LSPR mode located at 2.138 eV seem to be present all over the AuAg nanotube. Plasmon maps of two other LSPRs of different polar modes located at 2.29 eV and 2.385 eV are also shown in this figure.

As it is discussed intensely in the previous chapter on the cuboid AuAg nanostructures, presence of a substrate splits the LSPR modes into proximal and distal modes [91]. In Fig. 4.16, we show the BEM simulated plasmon maps of the AuAg nanotube obtained by the beam incident on the pentagonal cross-section in order to have a better understanding about the proximal and distal modes. As seen in this figure, cross-sectional plasmon maps of the 8 different modes (whose planar views are presented in Fig. 4.15) are shown, where the 15 nm thick substrate is clearly visible. First and second order Fabry-Perot modes, located at 0.504 eV and 0.979 eV, respectively, have a homogeneous distribution all around, both at the inner and outer parts of, the AuAg nanotube. However, third and fourth order Fabry-Perot modes located at 1.359 eV and 1.625 eV have a highly intense distribution confined to the lower parts (which are in contact with the substrate) of the nanotube suggesting that these modes can be considered as kind of proximal modes. The first LSPR mode located at 1.891 eV is a proximal mode, which has a more or less homogeneous distribution of plasmon resonances along inner and outer parts of the nanotube wall. Other three LSPR modes located at 2.138 eV, 2.29 eV and 2.385 eV can be clearly identified as distal modes from these cross-sectional plasmon maps. It is shown that the mode located at 2.29 eV is confined at the distal corner with

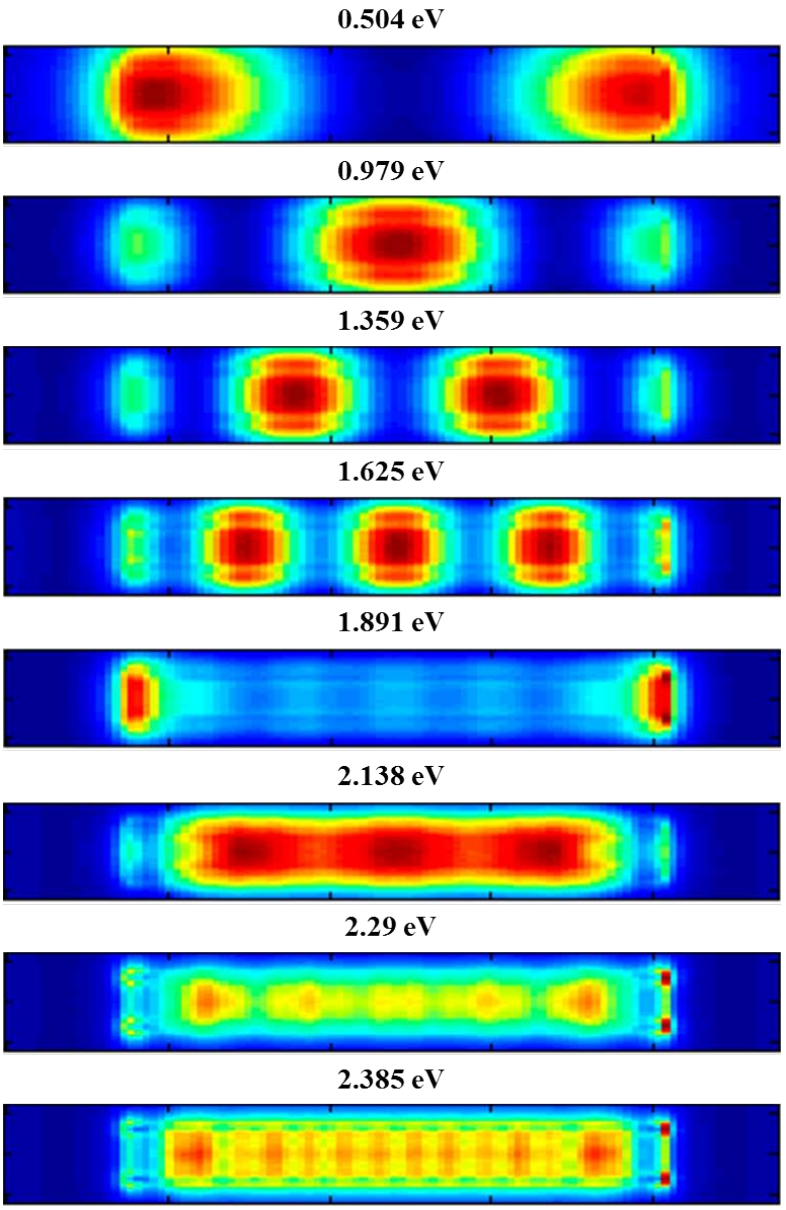

FIGURE 4.15: BEM simulated plasmon maps of the AuAg nanotube standing on a Si_3N_4 substrate: Maps of 8 different modes, located at 0.504 eV, 0.979 eV, 1.359 eV, 1.625 eV, 1.891 eV, 2.139 eV, 2.29 eV and 2.385 eV, are presented.

some contributions from the upper edges, whereas the mode located at 2.385 eV is kind of an edge LSPR mode generated from the distal edges.

Fig. 4.17 shows the BEM simulated 3D EM field maps the different plasmon peaks of the AuAg nanotube, which are located at 0.55 eV, 0.99 eV, 1.36 eV, 1.62 eV, 1.89 eV, 2.14 eV, 2.29 eV and 2.385 eV. These maps are obtained with a beam excitation at the near-edge, at x = 0 nm and y = -10 nm at the scales shown for the individual EM field maps, except the ones located 2.14 eV and 2.385 eV which are obtained with a beam excitation at the center of the nanotube (x = 332.5 nm and y = 84 nm). The EM field maps presented on the left are 4 Fabry-Perot modes. The highly confined EM field at

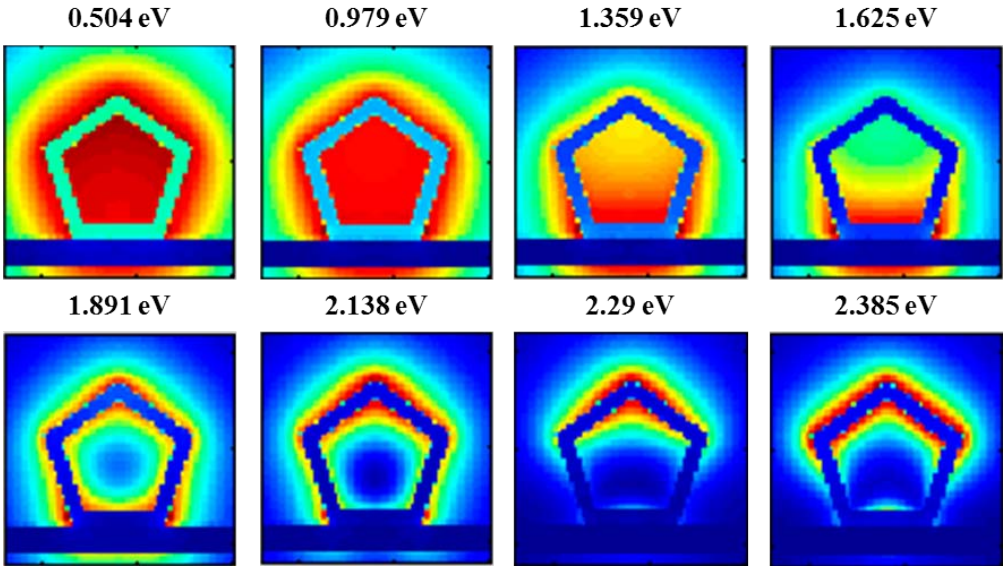

FIGURE 4.16: BEM simulated plasmon maps of the AuAg nanotube obtained by the beam incident on the pentagonal cross-section: Maps of 8 different modes, located at 0.504 eV, 0.979 eV, 1.359 eV, 1.625 eV, 1.891 eV, 2.139 eV, 2.29 eV and 2.385 eV, are presented.

the tip with larger values for the LSPR mode located at 1.89 eV is worth noting. The EM field maps of the modes located at 2.14 eV and 2.385 eV, which are obtained by a beam excitation in the middle of the nanotube, suggest that these modes are kind of edge LSPR modes of the pentagonal nanotube.

TABLE 4.4: Comparison of the plasmon components obtained experimentally by Gaussian fitting and VCA routines and obtained by BEM simulations for the completely hollow AuAg nanotube.

	Gaussian fitting	**VCA**	**BEM**
1^{st} component	0.45-0.60 eV	∼0.5 eV	0.504 eV
2^{nd} component	0.8-1.1 eV	∼0.9 eV	0.979 eV
3^{rd} component	1.1-1.5 eV	∼1.2 eV	1.359 eV
4^{th} component	1.5-2.3 eV	∼1.5 eV	1.625 eV
5^{th} component	2.3-3.1 eV	∼1.9 eV	1.891 eV
6^{th} component			2.138 eV
7^{th} component			2.29 eV
8^{th} component			2.385 eV

Table 4.4 shows the comparison of plasmon resonances for the completely hollow AuAg nanotube. Experimentally obtained results by two different routines of Gaussian fitting (Fig. 4.4) and VCA (Fig. 4.5) are listed in this table, along with the results obtained by BEM simulations (Fig. 4.15). The energy values of the components for the Gaussian

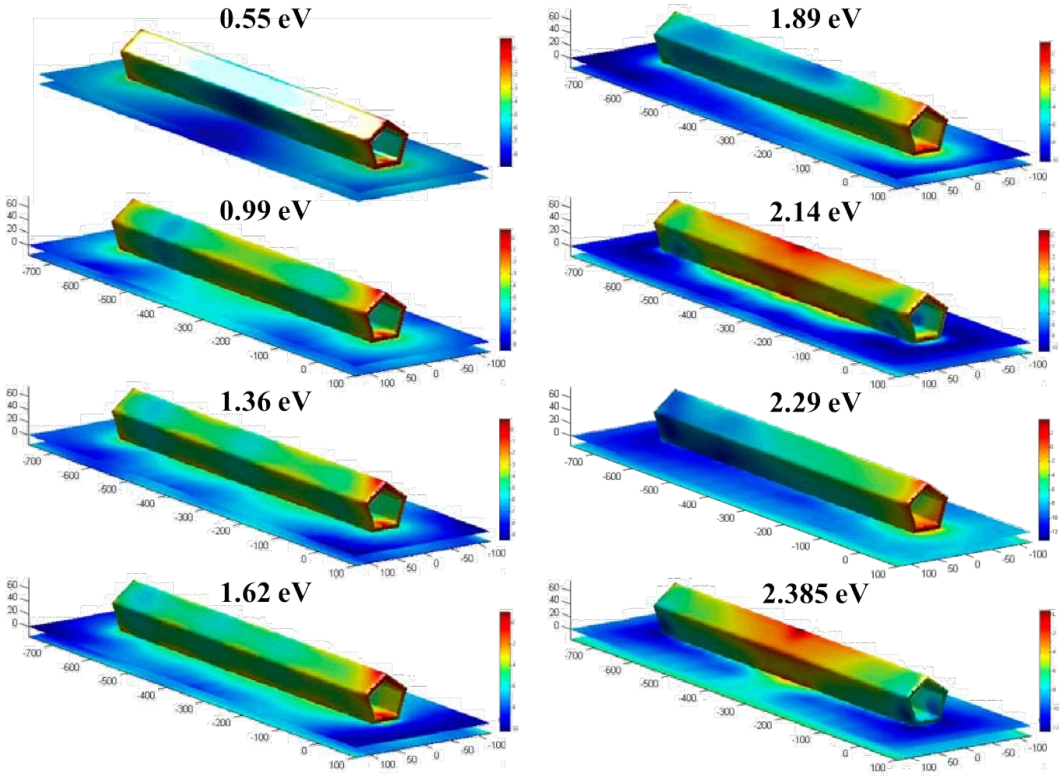

FIGURE 4.17: BEM simulated 3D EM field maps of the different plasmon peaks of the AuAg nanotube, which are located at 0.55 eV, 0.99 eV, 1.36 eV, 1.62 eV, 1.89 eV, 2.14 eV, 2.29 eV and 2.385 eV. These maps are obtained with a beam excitation from the near-edge (x = 0 nm, y = -10 nm), except the ones at 2.14 eV and 2.385 eV, which are obtained with a beam excitation at the center of the nanotube.

fitting are given as ranges of energies, which indicated the range of peak fitting. One can see from this table that, plasmon results obtained by 3 different routines are qualitatively in agreement. It should be pointed out that the energies of the Fabry-Perot modes obtained by VCA are slightly lower than those obtained by BEM simulations. For instance, fourth order Fabry-Perot mode is experimentally found to be located at ∼1.5 eV by VCA, whereas BEM simulation reveals that it is located at 1.625 eV. Moreover, LSPR component of the VCA analysis (component V) is located at 1.9 eV, yet it is a wide peak covering the energy range between ∼1.5 eV and 2.5 eV. One can suggest that 4 different LSPR modes obtained by BEM simulations between 1.891 eV and 2.385 eV are represented along this wide peak of the VCA.

4.3 Hybrid AuAg nanotubes

In this section, we present structural and plasmonic properties of another type of the AuAg nanotubes, so-called hybrid AuAg nanotubes which comprise sequential arrays of solid Ag and hollow AuAg parts.

4.3.1 Structural characterization

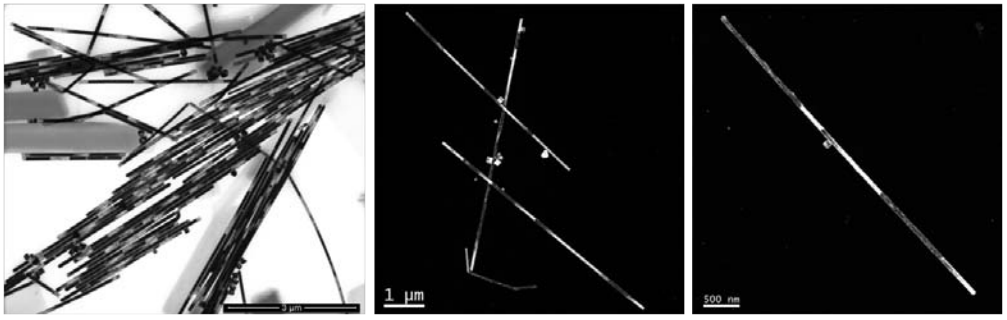

FIGURE 4.18: Bright field STEM and HAADF STEM micrographs taken from the hybrid AuAg nanotubes, revealing the presence of several micron long hybrid nanotubes formed by arrays of solid and hollow parts.

Fig. 4.18 shows a bright field STEM micrograph and two HAADF STEM micrographs revealing the hybrid nature of the nanotubes with their sequential solid and hollow parts. As seen in these figures, hybrid AuAg nanotubes have lengths of several micron. Although the presence of clearly formed hollow parts are obvious as a result of the site specific galvanic replacement reaction, it is also evident that the periodicity between hollow and solid parts by means of length could not be controlled.

Fig. 4.19 shows several HRTEM micrographs taken from a hybrid AuAg nanotube. HRTEM micrographs presented in the upper row reveal the sharp tip of the nanowire with its multitwinned structure. A lighter contrast region with a shell-like structure is also visible in these HRTEM micrographs, which is an Au-rich layer, with a thickness of about 9 nm, deposited during the applied galvanic replacement reaction with a mechanism similar to the Ag@Au core-shell nanocubes of the previous chapter. The HRTEM micrographs presented in the lower row are taken from the interfaces between solid and hollow parts and clearly reveal that Ag etching during the galvanic replacement reaction took place with an atomic layer precision.

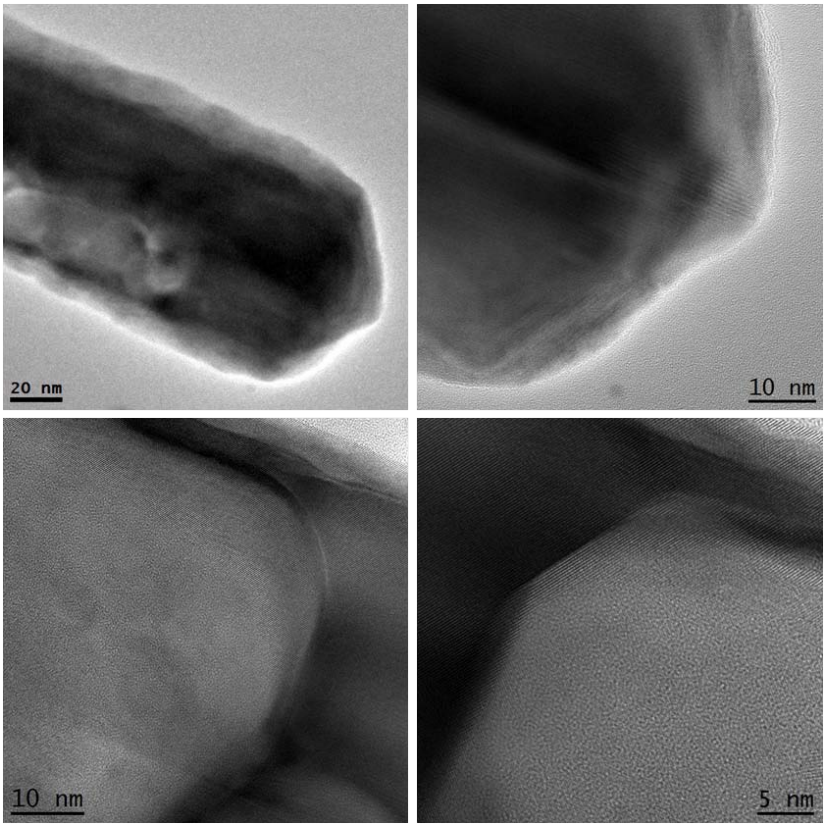

FIGURE 4.19: HRTEM micrographs taken from a hybrid AuAg nanotube, showing the crystallinity and sharp interfaces between the solid and hollow parts of the nanotubes.

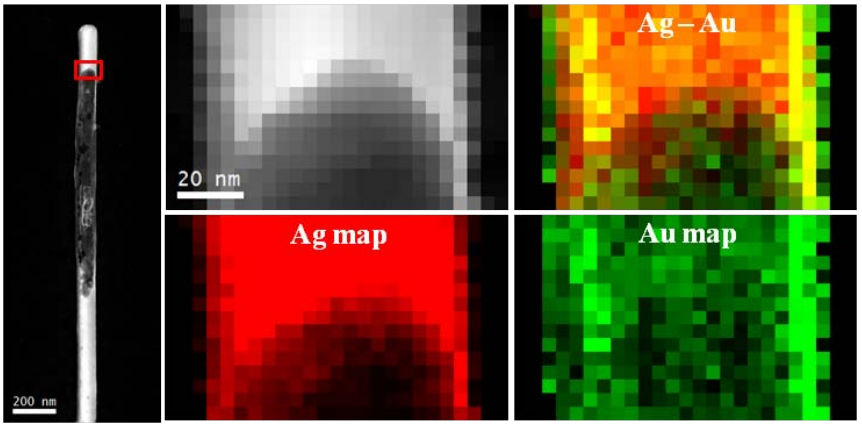

FIGURE 4.20: HAADF STEM micrograph of a hybrid AuAg nanotube with a $\sim$ 90 nm diameter. EDX maps of the red rectangular region: Simultaneous HAADF STEM, elemental Ag (in red) and Au (in green) maps and their composite.

Figures 4.20 and 4.21 show STEM-EDX studies conducted on two different hybrid AuAg nanotubes and reveal the elemental distribution of Ag and Au throughout the interfaces between hollow and solid parts. Fig. 4.20 shows a HAADF STEM micrograph of a hybrid AuAg nanotube with $\sim$ 90 nm diameter and elemental EDX maps of the red rectangular region over a sharp interface where simultaneous HAADF STEM micrograph

of the region of interest, elemental Ag (red) and Au (green) maps and their composite are presented. Similarly, Fig. 4.21 shows STEM-EDX studies conducted on a "wormhole" like interface of a hybrid AuAg nanotube with a $\sim$ 88 nm diameter. As seen in both of these figures, solid parts are notably Ag-rich, whereas the hollow parts and outer shells seem to be Au-rich.

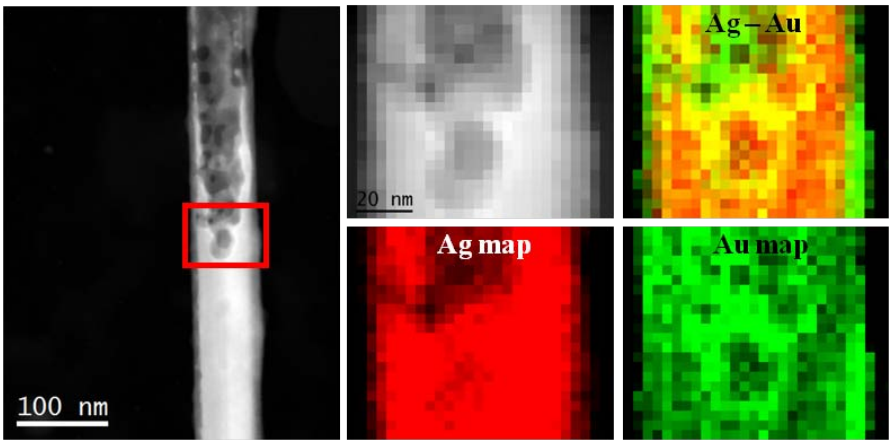

FIGURE 4.21: HAADF STEM micrograph of a hybrid AuAg nanotube with a $\sim$ 88 nm diameter. EDX maps of the red rectangular region: Simultaneous HAADF STEM, elemental Ag (in red) and Au (in green) maps and their composite.

In Fig. 4.22, we show a STEM-EDX line scan across a length of about 4 μm for a hybrid AuAg nanotube with a $\sim$ 88 nm diameter. The inset in the HAADF STEM micrograph corresponds to the EDX intensities of Ag (red) and Au (green), which are normalized to 100 and represented in arbitrary units. As seen in this figure, similar to the above presented STEM-EDX maps, solid parts are Ag-rich and the intensities of Au peaks increase significicantly in the hollow parts.

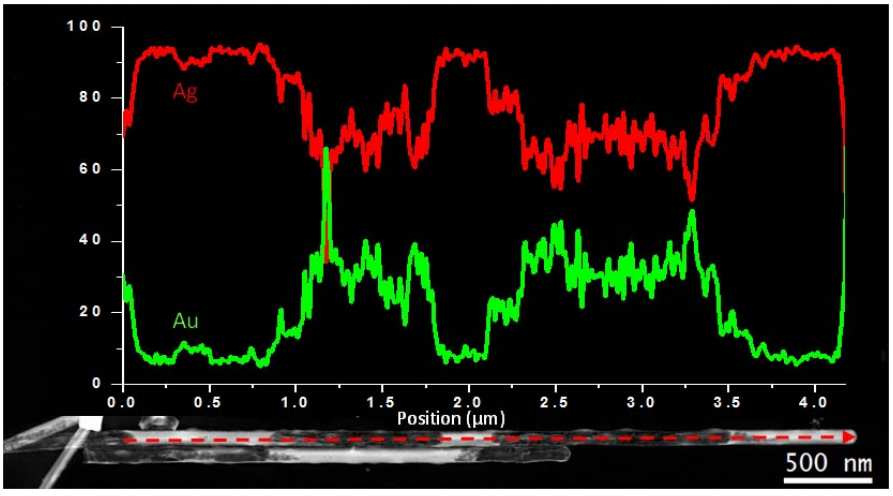

FIGURE 4.22: HAADF STEM micrograph of a hybrid AuAg nanotube with a diameter of 88 nm. Inset shows the EDX line scan results (intensities are arbitrary units and normalized) obtained through the red arrow.

4.3.2 Local plasmonic properties

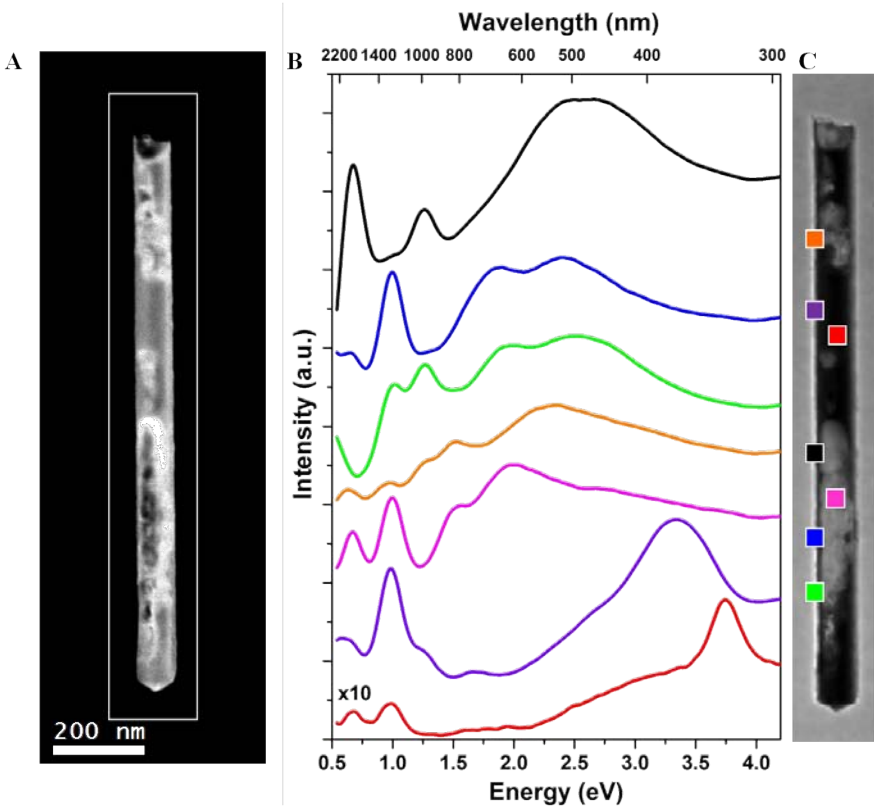

FIGURE 4.23: A. HAADF STEM micrograph of a hybrid AuAg nanotube, which is 89 nm in diameter and 1.24 μm in length. B. Background subtracted selected area EEL spectra of different locations marked in C, which is the EELS SI taken from the white rectangle in A

As seen in the above presented micrographs, hybrid AuAg nanotubes have lengths of several micron, which is quite impractical for nanoscale EELS mapping due to the long acquisition time and stability (drift) issues. Therefore, we have tried to choose an individual nanotube that is shorter yet keeps the general features of the hybrid structure. Fig. 4.23A shows a 1.24 μm long hybrid AuAg nanotube with a diameter of 89 nm, where we have obtained EELS SI over the area indicated with a white rectangle. Fig. 4.23B shows background subtracted selected area EEL spectra of different locations indicated in Fig. 4.23C, which is the EELS SI obtained from the region marked with a white rectangle in Fig. 4.23A. As seen in Fig. 4.23B, this hybrid AuAg nanotube contains multiple plasmon resonances with energies from $\sim$ 0.6 eV to 3.8 eV. One can observe the plasmon peaks located at $\sim$0.7 eV, $\sim$1.0 eV, $\sim$1.26 eV, $\sim$1.5 eV, $\sim$1.86 eV, $\sim$2.4 eV, $\sim$3.36 eV and $\sim$3.78 eV which are present at different parts of the nanotube. Among these various plasmon modes, the ones at lower energies such as the peaks shown in the EEL spectra obtained from the black, blue and green areas, seem to be Fabry-Perot like resonator modes. Some other modes mostly probably corresponding to the Au-rich

related LSPR modes or LSPR mode of Ag can be seen in the EEL spectra obtained from the pink and purple regions, respectively. Bulk plasmon mode of Ag located at ∼3.8 eV is clearly visible in the EEL spectrum obtained from the solid part indicated with a red square.

4.3.3 Processing of plasmonic properties

Fig. 4.24 shows the plasmon energy maps (left) and their corresponding intensity maps (right) fitting a Gaussian to the energy ranges between 0.6-0.75 eV, 0.9-1.1 eV, 1.1-1.5 eV, 1.45-1.65 eV, 1.7-2.7 eV, 2.9-3.6 eV, and 3.5-3.9 eV in the EELS SI obtained from the hybrid AuAg nanotube. As seen in these maps, the plasmon mode with lowest energy (between 0.6 and 0.75 eV) is the second order Fabry-Perot type resonator mode. This is due to the fact that we could not subtract the background of the EEL spectra by using the power law such that it would let us to observe the first order mode, as this mode is located at energies lower than 0.5 eV, the smallest energy we could obtain by power law background subtraction routine. Third and fourth order modes are clearly visible in the plasmon energy and intensity maps between 0.9-1.1 eV and 1.1-1.5 eV, respectively. The plasmon mode mapped between 1.45 and 1.65 eV might be the fifth order resonator mode but some parts of the nanotube do not have plasmon excitation, which makes it hard to comment on whether it is a resonator mode according to the results obtained by Gaussian fitting. A wide Gaussian is fitted between the energy ranges of 1.7 and 2.7 eV in order to cover LSPR modes associated to the hollow parts and their distribution is shown in the plasmon energy and intensity maps of Fig. 4.24. Another LSPR mode is mapped between 2.9 and 3.6 eV and its distribution reveals that this mode is the LSPR mode of Ag as it is only present around the solid parts. Map of bulk plasmon mode of Ag is obtained by fitting a Gaussian between 3.5 and 3.9 eV and clearly reveals the regions consist of pure Ag throughout the hybrid AuAg nanotube.

Fig. 4.25 shows the 8 different plasmon components and their corresponding abundance maps obtained by applying VCA analysis to the EELS data of the hybrid AuAg nanotube. First thing to note in this figure is the EEL spectrum and plasmon map of the first order component that could not be observed by the above presented Gaussian analysis. It is located at 0.44 eV which corresponds to ∼2818 nm (in short wavelength infrared region). The components obtained by VCA revealed that second, third and fourth order resonator modes (components II, III and IV) are located at ∼0.66 eV, ∼1.0 eV and ∼1.26 eV, respectively. As it is shown experimentally and by BEM simulations for the completely hollow AuAg nanotubes, Fabry-Perot modes are generated highly intensely inside the hollow nanotubes. The abundance map of the third order Fabry-Perot mode (component III) clearly confirms such a behavior in hybrid AuAg nanotubes, where the

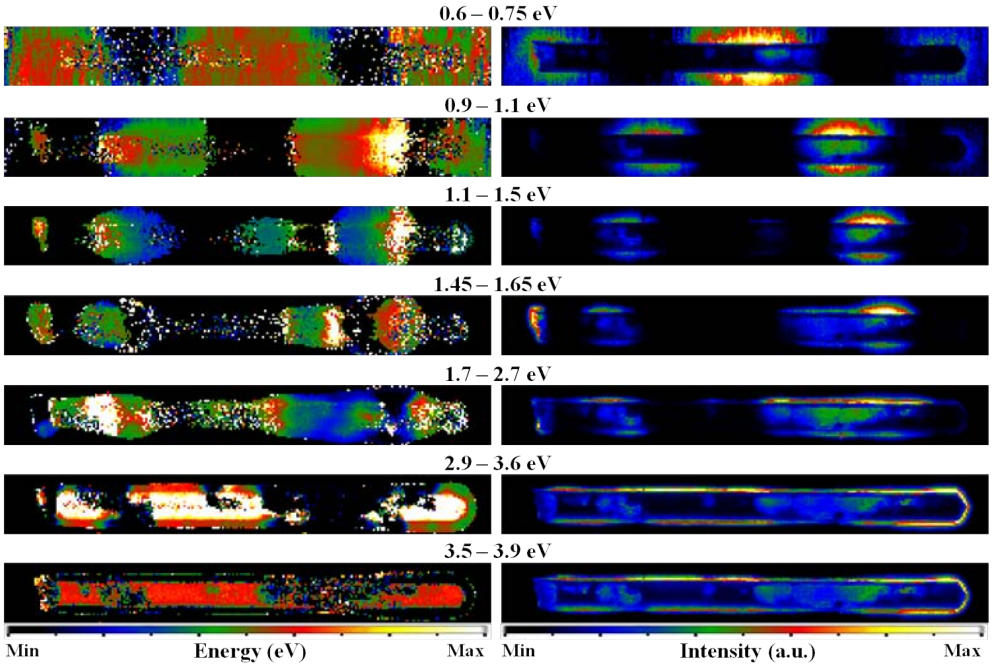

FIGURE 4.24: Plasmon energy maps (left) and their corresponding intensity maps (right) obtained by fitting a Gaussian to the energy ranges between 0.6-0.75 eV, 0.9-1.1 eV, 1.1-1.5 eV, 1.45-1.65 eV, 1.7-2.7 eV, 2.9-3.6 eV, and 3.5-3.9 eV. White pixels in the energy maps are out of fitting parameters.

same mode has much higher intensity at the hollow part (on the right) compared to the solid part (on the left) along the same nanotube. We have questioned the possibility of the plasmon mode located at ∼1.6 eV being a resonator mode on the results obtained by Gaussian fitting. However, the component V of the Fig. 4.25 and its corresponding abundance map suggests that this mode as a LSPR mode which is mostly confined at the hollow tip. A component located at ∼2.3 eV, covering a quite wide range of energies between 1.6 and 3.1 eV is obtained (component VI) by VCA and its corresponding abundance map reveals that this component is associated with the LSPR mode of the hollow parts. Components related to the surface and bulk plasmon resonances of Ag are presented in components VII and VIII, respectively, along with their distribution.

We should point out that due to its long size and complex structure, we could not obtain BEM simulations on the hybrid nanotube. We present the comparison of different modes obtained experimentally by Gaussian fitting and VCA routines for the hybrid AuAg nanotube in Table 4.5. Again, energy values of the components obtained by Gaussian fitting are presented as energy ranges. 7 different components obtained by Gaussian fitting and 8 different components obtained by VCA are listed in this table. It is important to note that with VCA, we could map first order Fabry-Perot mode located at 0.44 eV, which was not possible to map with Gaussian fitting as we could not extract this peak by using the power-law background subtraction algorithm.

It is worth pointing out that hybrid AuAg nanotubes contain plasmon resonance in a wide range of energies from ∼0.4 eV to ∼3.8 eV. We anticipate that this type of hollow nanostructures may found applications in photoactive devices such as solar cells and photodetectors, where plasmon enhanced light absorptions significantly increase the performance of such devices. Moreover, if, by having better control over the synthesis, the sequence of the hollow and solid parts can be controlled, they could make valuable contributions to the fields where the control and manipulation of light over wide ranges are essential.

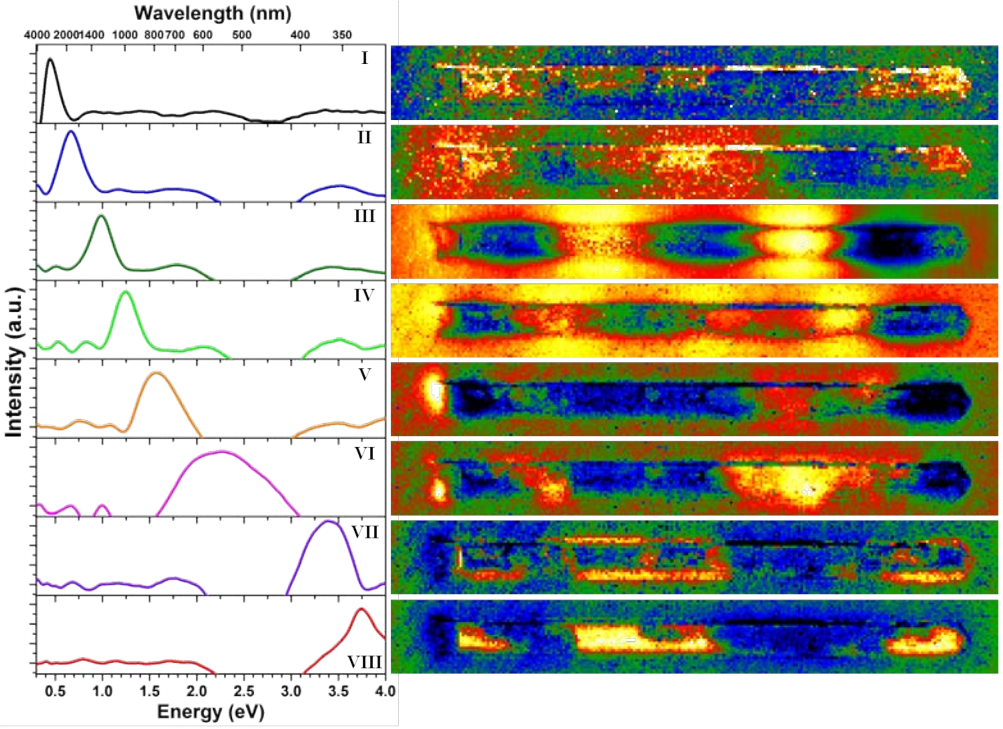

FIGURE 4.25: VCA of the hybrid AuAg nanotube: Plasmon components and their corresponding abundance maps.

TABLE 4.5: Comparison of the plasmon components obtained experimentally by Gaussian fitting and VCA routines for the hybrid AuAg nanotube.

	Gaussian fitting	**VCA**
1^{st} component	0.60-0.75 eV	∼0.44 eV
2^{nd} component	0.9-1.1 eV	∼0.66 eV
3^{rd} component	1.1-1.5 eV	∼1.0 eV
4^{th} component	1.45-1.65 eV	∼1.26 eV
5^{th} component	1.7-2.7 eV	∼1.6 eV
6^{th} component	2.9-3.6 eV	∼2.3 eV
7^{th} component	3.5-3.9 eV	∼3.4 eV
8^{th} component		∼3.76 eV

4.4 Summary and conclusions

In this chapter, the plasmonic properties of hollow 1D nanostructures are presented. Bimetallic AuAg nanotubes are synthesized via galvanic replacement process where the Ag nanowires are used as a template resulting in the formation of nanotubes, which is quite similar to the nanobox synthesis presented in Chapter 3. We have prepared two different samples consisting of completely hollow and hybrid AuAg nanotubes, respectively. The hybrid nanotubes are a sequence formation of solid Ag core with AuAg shell and hollow AuAg parts. The samples are deposited on 15 nm thick Si_3N_4 grids and their plasmonic properties are investigated by means of EELS using a monochromated STEM operated at 80 kV. In addition to the plasmonic properties, we present structural features of the completely hollow AuAg nanotubes and hybrid AuAg nanotubes by means of HRTEM investigations. Detailed STEM-EDX characterization of the hybrid AuAg nanotubes are also presented. BEM simulations on the completely hollow AuAg nanotubes are conducted.

We have shown the plasmonic properties of a completely hollow AuAg nanotube, presenting a length of 655 nm and a diameter of 84 nm with 10 nm thick walls. The AuAg nanotubes keep the multitwinned pentagonal shape of the Ag nanowires. The presence of several Fabry-Perot resonator modes and LSPR modes and their distribution are shown by Gaussian fitting and VCA, where Gaussian fitting revealed the presence of Fabry-Perot resonances up to third order and the fourth order mode could be revealed by VCA. It is shown that the plasmon modes, especially Fabry-Perot modes, are highly intense inside the nanotube.

BEM simulations on the 1D Ag nanostructures are conducted in order to investigate the plasmonic properties of solid and hollow 1D nanostructures and the effects of the substrate on the plasmonic properties of hollow 1D nanostructures. The plasmon resonances of solid Ag nanowires shifted to lower energies for the case of hollow Ag nanotubes due to plasmon hybridization between solid and cavity modes. Both nanostructures revealed the presence of multiple Fabry-Perot and LSPR modes, where the LSPR modes were, mostly, homogeneously distributed for the nanotube. It is worth noting that the presence of a dark plasmonic breathing-like mode has been observed during the simulations of Ag nanowire, which wasn't present for the experimental analyses conducted on the nanotubes. As discussed above, the presence and the origin of this mode needs to be studied in more detail, which we plan to do in the near future. The distribution of the plasmon resonances along the planar and cross-sectional views revealed the presence of highly intense resonances inside the nanotube. Ag nanotube on Si_3N_4 substrate had plasmon resonances at slightly lower energies except the first order Fabry-Perot mode, compared to those obtained at an Ag nanotube standing in vacuum. Finally, we have

simulated an AuAg nanotube composed of 60 at.% Au and 40 at.% Ag with the same sizes as the experimentally investigated hollow AuAg nanotube. It has been seen that the higher energy (> 2.5 eV) plasmon resonances observed for the Ag nanostructures are not present at the AuAg nanotube due to the fact that Au suffers interband transitions at these energy range (which is discussed in Chapter 1). An accurate fit between the results obtained by VCA and BEM simulation has been achieved.

The presence of multiple Fabry-Perot modes and LSPR modes are observed on a 1.24 μm long hybrid AuAg nanotube with a diameter of 89 nm. It is worth noting that different LSPR modes corresponding to the hollow parts and solid Ag parts are obtained by using both Gaussian fitting and VCA routines. The distribution of Fabry-Perot resonances up to fourth order are shown, where the hollow parts of the hybrid nanotube had much intense resonances thanks to the resonances located inside the nanotube. As the simulation of AuAg hybrid nanotubes would require too complex models and longer comptuing times, which are out of our computing possibilities at the moment, we could not obtain simulation results for this promising structure. Nevertheless, we do not discard to work on such a demanding models in near future.